Applied Clay Science 213 (2021) 106241

Contents lists available at ScienceDirect

Applied Clay Science

journal homepage: www.elsevier.com/locate/clay

Removal of iodide from water using halloysite/Ag_2O composites as efficient adsorbent

Wenbin Yu [a,b], Quan Wan [a,b,c,*], Daoyong Tan [d], Shuguang Yang [a,b], Zonghua Qin [a,b], Xin Nie [a,b]

[a] State Key Laboratory of Ore Deposit Geochemistry, Institute of Geochemistry, Chinese Academy of Sciences, Guiyang, Guizhou 550081, China
[b] University of Chinese Academy of Sciences, Beijing 100049, China
[c] CAS Center for Excellence in Comparative Planetology, Hefei 230026, China
[d] Key Laboratory of Solid Waste Treatment and Resource Recycle, Ministry of Education, Southwest University of Science and Technology, Sichuan, Mianyang 621010, China

ARTICLE INFO

Keywords:
Nuclear Waste
Iodide
Adsorption
Halloysite
Ag_2O
Composite

ABSTRACT

The efficient removal of iodide (I^-) from water is challenging to accomplish because of the large size and low charge of I^-. In this study, halloysite/Ag_2O composites were prepared, characterized, and used to remove I^- from water. The Ag_2O nanoparticles primarily resided in the lumen of halloysite in the composites, whose amount and size can be readily controlled by adjusting the concentration of Ag^+ during the preparation process. Moreover, there is rapid adsorption of I^- by the composites, whose kinetics followed a pseudo-second-order model. With a solid/liquid ratio of 50 mg/20 mL and an initial pH of 7.5 ± 0.2, the maximum I^- adsorption capacity of composites with an approximately 0.98% and 2.42% Ag_2O content was 13.7 mg/g and 39.99 mg/g, which is 48 and 142 times higher than that of raw halloysite, respectively. Importantly, the composites exhibited high selective adsorption to I^-, and their I^- removal efficiency is barely affected by the presence of Cl^-, Br^-, or SO_4^{2-}. The high adsorption capacity of the composite is driven by the small particle sizes of Ag_2O due to the spatial confinement of the lumen of halloysite and the newly formed nanopores between Ag_2O particles and the inner wall of halloysite. After capturing the radioactive I^-, the composites are expected to constitute a low radiological hazard because of the shielding provided by the halloysite wall. Taken together, these results suggest the halloysite/Ag_2O composites could be a promising adsorbent suitable for use in the efficient removal of radioactive I^- from nuclear wastewater.

1. Introduction

Radioactive iodine, a by-product of uranium fission, can be released into water, soils, and atmosphere through nuclear weapon tests, nuclear medicine treatments, and especially via nuclear accidents, such as those which occurred at Three Mile Island in the USA in 1979, at Chernobyl in Russia in 1986, and at Fukushima in Japan in 2011. The Fukushima Daiichi accident released 1.5×10^7 kg ^{131}I into the environment (Von Hippel, 2011). Further, radioiodine is potentially problematic in groundwater at radiological waste disposal sites. For example, radioiodine has been identified as a risk at the Hanford and the Savannah River sites in the USA, where its concentration in groundwater is well above the drinking water standard (Kaplan et al., 2014). This is a hazard because the radioiodine in water is easily ingested by humans through food chain which causes a number of health problems. It is well known that exposure to even small amounts of radioactive iodine can lead to an increase in metabolic disorders, mental retardation, and thyroid cancer in humans (Theiss et al., 2016; Yu et al., 2020). Therefore, carrying out the efficient removal of radioactive iodine from water is a task of great importance.

In aqueous environments, when natural organic matter is limited, iodine exists primarily as iodide (I^-) and iodate (IO_3^-) depending on the redox conditions and pH (Yu et al., 2019). Of these two species, I^- is more commonly found in suboxic to reducing conditions with a wide pH range of 4–10 in natural water environment (Fuge and Johnson, 2015). In the last decades, much research has focused on how to remove I^- from water, for which different methods were tried, such as adsorption (Choung et al., 2013), photocatalysis (Wang et al., 2019), oxidation

* Corresponding author at: State Key Laboratory of Ore Deposit Geochemistry, Institute of Geochemistry, Chinese Academy of Sciences, Guiyang, Guizhou 550081, China.
E-mail address: wanquan@vip.gyig.ac.cn (Q. Wan).

https://doi.org/10.1016/j.clay.2021.106241
Received 17 June 2021; Received in revised form 27 July 2021; Accepted 3 August 2021
Available online 17 August 2021

(Bichsel and Von Gunten, 1999), and membrane electrolysis (Tanno et al., 1986), to name a few. Among them, adsorption is currently the most applicable technology because of the system's flexibility, low energy input, and inexpensive operation costs (Choung et al., 2013; Yu et al., 2015a).

Different adsorbents, such as activated carbon (Hoskins et al., 2002), anion exchange resins (Decamp and Happel, 2013), natural minerals (Morimoto et al., 2011; Yu et al., 2019), metal (Ag, Hg, or Cu(I)) compounds (Balsley et al., 1996; Liu et al., 2015; Liu et al., 2016), and silver oxide composites (Yang et al., 2011; Bo et al., 2013), have been reported capable of removing radioactive I^-. In a recent paper, covalent organic framework-based materials as adsorbents to radioactive I^- and other pollutants was critically reviewed (Liu et al., 2021). Remarkably, the Ag_2O-composites featuring Ag_2O nanoparticles dispersed upon carriers, such as nanotubes (Yang et al., 2011), nanofibers (Yang et al., 2008), nanolaminas (Bo et al., 2013), or 3D spheres (Liu et al., 2015), are considered very attractive because of their high adsorption capacities and the strong affinity between I^- and silver. Yet for almost all the reported Ag_2O-composites (Yang et al., 2008; Yang et al., 2011; Bo et al., 2013; Liu et al., 2015), the Ag_2O nanoparticles existed on the external surface of the carriers, which may lead to Ag_2O nanocrystals readily detaching from the carriers in some circumstances. On the other hand, in the process of preparing those reported Ag_2O-composites, it is usually necessary to first synthesize the carriers (Yang et al., 2011; Liu et al., 2015), rendering the preparation process of Ag_2O-composites both cumbersome and costly.

Halloysite ($Al_2(OH)_4Si_2O_5{\cdot}2H_2O$) is a naturally occurring dioctahedral 1:1 clay mineral with a unique nanotubular morphology, being inexpensive and readily available worldwide (Joussein et al., 2005). Its nanosized tubular morphology results from the wrapping of layers that is driven by the mismatch between the smaller octahedral sheet and larger tetrahedral sheet in the 1:1 layer (Bates et al., 1950; Tan et al., 2013). Generally, tubular halloysite is ca. 0.02–30 μm in length and has an external diameter that varies from ca. 30 to 190 nm, with an internal diameter of ca. 10–100 nm (Yuan et al., 2015). These sizes of tubular halloysite vary according to different deposits whose genesis and occurrence conditions differ (Pasbakhsh et al., 2013). Given its special nanosized tubular morphology, the specific surface area and pore volume of halloysite normally exceed those of other clay minerals (such as kaolinite), making it an excellent carrier to load with various chemical species, such as adsorbent (Wei et al., 2019), drugs (Tan et al., 2015), catalysts (Zeng et al., 2017), and even antibacterial agents (Shu et al., 2017). In particular, the lumen size of halloysite is greater than 10 nm, so it is sufficiently large to accommodate nanoparticles. In recent years, not only Ag nanoparticles and nanorods (Ouyang et al., 2016; Zeng et al., 2017) but also copper-nickel alloy nanoparticles (Abdullayev et al., 2011) and carbon nanodots (Wu et al., 2017) were successfully loaded into the lumen of halloysite; the generated composites have sound structural stability and notable corresponding catalytic, scavenging or antibacterial properties. To our best knowledge, however, there are no reports yet on the preparation of a halloysite/Ag_2O composite as an adsorbent for the removal of radioactive I^-.

In the present work, halloysite/Ag_2O composites were prepared, in which Ag_2O nanoparticles were primarily loaded into the lumen of halloysite. The prepared composites were characterized by various techniques and used as adsorbents to radioactive I^- from water. Because Ag_2O nanoparticles primarily resided in the lumen of halloysite, the halloysite/Ag_2O composites possessed high structural stability, and it is anticipated that after capture of the radioactive I^- the composites will show a low radiological hazard, due to shielding from the halloysite wall. The fundamental knowledge derived from this study is important for potential applications of halloysite for radioactive pollution control and the development of new efficient adsorbents in the future.

2. Materials and methods

2.1. Chemicals and materials

Crystalline potassium iodide (KI) (Sigma-Aldrich) was used as the source of I^-. Non-radioactive iodine (^{127}I) was used in the I^- uptake experiments because it has the same chemical reaction properties as radioactive iodine (Ikari et al., 2015; Yang et al., 2011). $AgNO_3$ (AR Grade), KCl (AR Grade), NaOH (AR Grade), and 68.0% HNO_3 were all purchased from Sinopharm Chemical Reagent Co., Ltd. Deionized water (resistivity, 18.2 MΩ·cm) was used in all the experiments. All chemicals were used as received, without further purification. The raw halloysite sample was collected from Danjiangkou, Hubei Province, China. The sample was purified by hand-selecting to remove the visible impurities (such as ferrites with the brown color), then dried at 120 °C overnight and ground. The resultant powder sample is referred to hereon as Hal.

2.2. Preparation of the halloysite/Ag_2O composites

Each halloysite/Ag_2O composite was prepared according to the following procedures: 1 g of dried Hal powder was placed into a chamber, and the chamber then vacuumized using a pump for 3 h to remove the air from the lumen of halloysite; after that, 100 mL $AgNO_3$ solution with designated concentration was dropped into the chamber via a funnel with a stopcock under vacuum. Upon completing this addition of $AgNO_3$ solution, the stopcock was fully opened to connect the chamber to the air, and halloysite/silver nitrate suspension was stirred for 3 h, to ensure the silver nitrate moved into the lumen of halloysite. The halloysite harboring the silver nitrate in its lumen was collected via filtering, after which 50 mL of a 0.01 mol/L NaOH solution was added, dropwise, onto the solid while vigorously stirring it. After stirring for 24 h, the solid was collected and washed thrice with deionized water, and then dried at 70 °C for 24 h, to yield the halloysite/Ag_2O composites (Hal-Ag_2O). Specifically, 0.2 mol/L and 0.5 mol/L of silver nitrate solution were used to prepare the halloysite/Ag_2O composites: these obtained composites were denoted as Hal-Ag_2O-1 and Hal-Ag_2O-2, respectively. For comparative purposes, Ag_2O nanoparticles (denoted as Ag_2O-NPS) were prepared by adding 0.1 mol/L of the NaOH solution into 0.1 mol/L of an $AgNO_3$ solution, using a procedure similar to that for the Hal-Ag_2O preparation.

2.3. Characterization

X-ray diffraction (XRD) data were collected on a Panalytical Empyrean multifunction X-ray diffractometer, equipped with a three-dimensional (3D) PIXcel detector. All the XRD patterns were collected at 40 kV and 40 mA using a continuous-scanning mode with a 0.026° step size and counting time of 30 s per step.

Transmission electron microscope (TEM) images were obtained using an FEI Tecnai G2 F20 S-TWIN microscope operated at an accelerating voltage of 200 kV. The specimens were prepared this way: samples were ultrasonically dispersed in ethanol for 5 min, then a droplet of the sample suspension was then dropped onto a lacy carbon-coated 200-mesh Cu grid which was left to stand for at least 10 min before being transferred into the microscope.

Low-temperature nitrogen (N_2) adsorption-desorption isotherms were measured using a Quantachrome Autosorb-iQ2-MP gas adsorption analyzer at a liquid-nitrogen temperature. Before their measurement, the samples were outgassed at 200 °C for 12 h under vacuum conditions. The total specific surface area of the sample, S_{BET}, was calculated from the N_2 adsorption data by using the multiple-point Brunauer-Emmett-Teller (BET) method (Brunauer et al., 1938), and the total pore volume, V_{total}, was evaluated based on the N_2 uptake at a relative pressure of ca. 0.99. The pore size distribution (PSD) curves were derived using the Barrett-Joyner-Halenda (BJH) method from the adsorption branch of the isotherms (Barrett et al., 1951).

X-ray photoelectron spectroscopy (XPS) analyses were performed using a Thermo Fisher Scientific Escalab 250 instrument equipped with a monochromatic Al Kα source and operated at 1486.8 eV while taking the measurements. The base pressure in the spectrometer analyzer chamber was below 5×10^{-8} mbar. The charge neutralizer filament was utilized during all experiments to control the charge of the samples. Spectra were collected from 0 to 1350 eV, using an X-ray spot size of 400 μm with a pass energy of 100 eV for the wide scan and 30 eV for individual elements. The quantitative analysis of XPS data was conducted in Thermo Avantage v5.934 software and the residual background was removed by implementing the Smart approach. All binding energies were referenced to the C1s line positioned at 284.8 eV.

2.4. Iodide adsorption experiments

A stock solution of I^- (5 mmol/L) was prepared by dissolving KI in deionized water. For the kinetics testing, a continuous technique is used that does not affect the time interval based continuous sampling. The experiment was performed by adding 0.5 g of adsorbent to 200 mL of the I^- solution, and this mixture was strongly shaken in a platform shaker to ensure its complete mixing. The adsorption time spanned 5 to 1440 min. At the end of each time interval, 0.5 mL of each suspension was taken and passed through a 0.22 μm PTFE filter. The residual aqueous I^- concentrations were determined using a Dionex ICS-90 Ion Chromatography (IC) system with an AG23 guard and AS23 analytical column, with a 14 mM Na_2CO_3/1.75 mM $NaHCO_3$ solution as the eluent.

The adsorption isotherms were obtained by carrying out batch adsorption experiments. In a typical run, 50 mg of adsorbent was added to 20 mL of an I^- solution with the scheduled concentration in a 50 mL centrifuge tube. Initial and final pH was measured using a pH meter. 0.1 M NaOH or 0.1 M HNO_3 was used to adjust the pH values of the suspensions. After a predetermined time for achieving adsorption equilibrium, the suspensions were centrifuged and ensuing their supernatants used for the I^- concentration analysis. The selective uptake of I^- by the composites was also tested in the presence of high concentrations of Cl^-, Br^-, or SO_4^{2-} anions. Specifically, 50 mg of adsorbent in 20 mL of aqueous solution containing 10 mM KCl (KBr, or K_2SO_4) and 1 mM KI was shaken for 24 h, then the concentration of I^- ions in the solution after adsorption was measured to determine the adsorption capacity of the adsorbent. All adsorption experiments were conducted at room temperature (25 ± 1 °C) unless otherwise noted, and each adsorption point was the average of duplicate or triplicate experiments. Blank experiments confirmed the absence of wall adsorption or I^- loss to volatilization.

The amount of I^- adsorbed per unit mass of the adsorbent at time t (h), q_t (mg/g) was calculated as follows:

$$q_t = (C_0 - C_t) \times M/m \quad (1)$$

where C_0 and C_t (mmol/L, mM) are the concentration of I^- in the reaction solution before and after adsorption for time t (h), respectively. M is the molar mass of I^-, and m (g) is the amount of adsorbent in 1 L of I^- solution. The I^- removal efficiency, E(%), was calculated using the following equation:

$$E(\%) = [(C_0 - C_t)/C_0] \times 100 \quad (2)$$

3. Results and discussion

3.1. Characterization of samples

The XRD pattern of Hal revealed that its main phase is 7 Å-halloysite with the 001 reflection at 0.74 nm (Fig. 1a). A minor amount of natroalunite impurity was also observed in the Hal sample, as indicated by the 012, 021, 113, and 303 reflections at 18.1°, 30.0°, 30.2°, and 48.0 (2θ), respectively (Fig. 1a). As seen in Fig. 1b, a new peak at 32.8° (2θ) appeared in the XRD pattern of Hal-Ag_2O-2, which can be attributed to

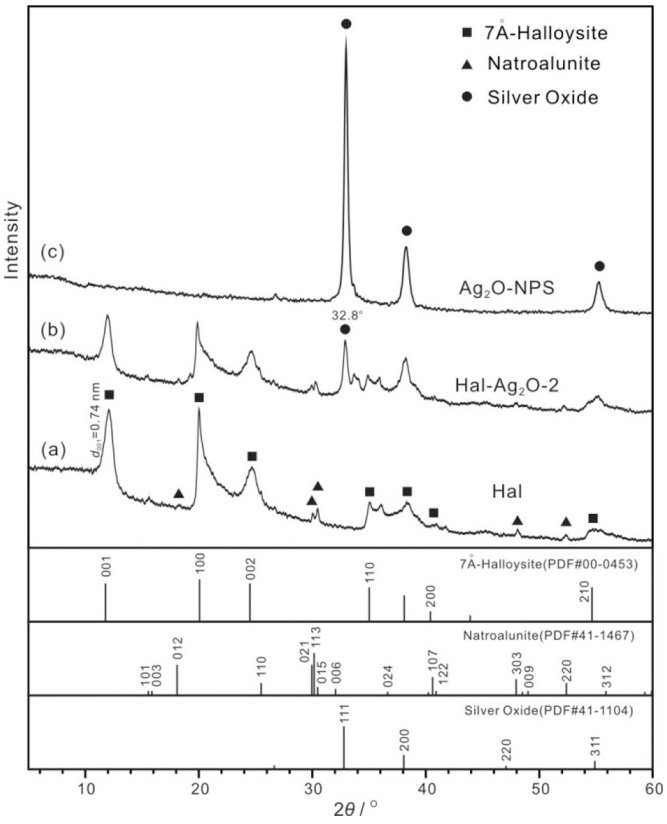

Fig. 1. XRD patterns of the halloysite (a), halloysite/Ag_2O composite (b), and Ag_2O nanoparticles (c).

the 111 reflection of silver oxide. This result indicated silver oxide was present in the halloysite silver oxide composite. However, the silver oxide cannot be detected on the XRD pattern of Hal-Ag_2O-1 (not shown), perhaps because of the ultra-fine size of its particles and its minor amount in this sample (see the following).

The XRD pattern of Ag_2O-NPS appears in Fig. 1c, it being consistent with the known diffraction pattern for silver oxide (Power Diffraction of File No. 41–1104) (Welton-Holzer et al., 1989). The diffraction lines of Ag_2O are broadened, thus indicating the Ag_2O particle is nanometer in size. The Scherrer formula ($D = k\lambda/\beta\cos\theta$) was used to evaluate the crystallite size of the Ag_2O particles, where k is the shape factor whose value is 0.89 (assuming that the particles are spherical), β is the integral breadth of the Bragg reflection, λ is the wavelength of the X-ray radiation, and θ is the Bragg angle (Burton et al., 2009). The calculated average particle size of Ag_2O was found to be 18.4 nm (See Table S1 in the Supporting Information).

The TEM image of Hal (Fig. 2a) clearly shows the halloysite particles are cylindrical in shape and contain a transparent central area that runs longitudinally along the cylinder, indicating that the halloysite particles were hollow and open-ended. As measured statistically from several TEM images (not shown), the length of Hal varies from 0.2 to 1.0 μm and the inner lumen diameter of Hal ranged from ca. 12 to 22 nm. It should however be noted that the accuracy of these dimensions is limited by the number of particles observed in the TEM images. For the halloysite/Ag_2O composites, Ag_2O nanoparticles were mainly existed in the inner lumen of halloysite nanotubes (Fig. 2b-d); a small amount of Ag_2O nanoparticles could also be found on the outer surface (Fig. 2b-c) and the edge surface (Fig. 2d) of the nanotubes. These results are directly attributable to the vacuumization process during the preparation of the composites. Assisted by atmospheric pressure, the aqueous silver nitrate solution could enter the lumen of halloysite, where the silver resource component would have been retained due to the capillary forces and finally converted into Ag_2O in the lumen of halloysite. In addition, the

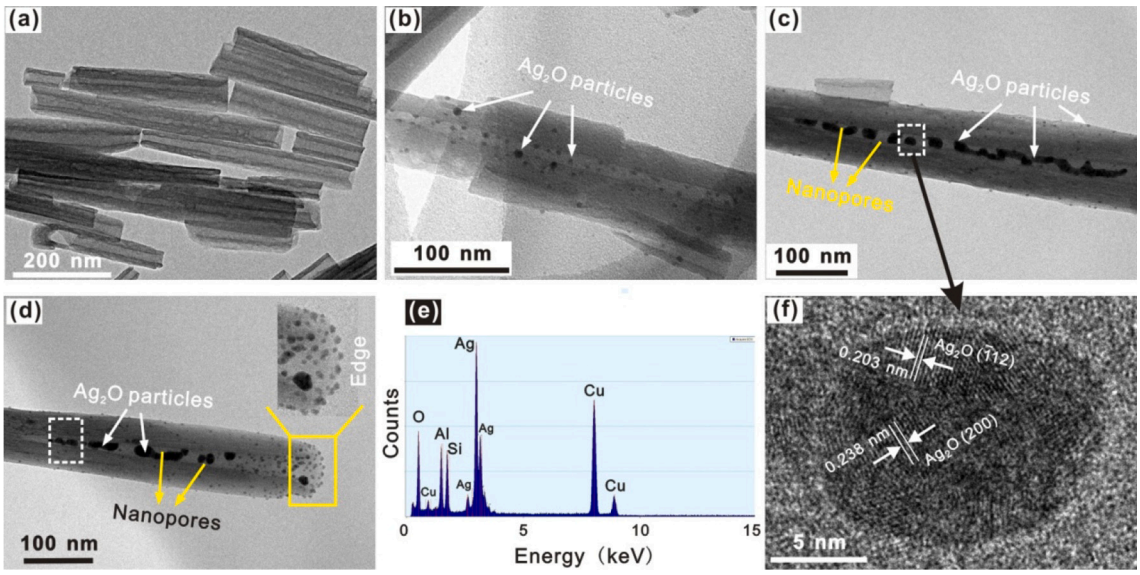

Fig. 2. TEM images of Hal (a), Hal-Ag_2O-1 (b), Hal-Ag_2O-2 (c-d), and the EDS spectrum of the prepared composite from the dashed square in *d* (e). (f) An HRTEM image of an Ag_2O crystal.

aluminum hydroxyl on the inner surface of halloysite could be adsorption sites for silver source, which is helpful to make the silver nitrate solution enter the lumen of halloysite. The Ag_2O nanoparticles found on the outer and edge surface is because there are also hydroxyl groups existed on the out surface (due to the crystallographic defects) and the edge surface of halloysite (Yuan et al., 2008), which could be adsorption sites for silver source (converted into Ag_2O finally). Compared with the Ag_2O nanoparticles in the lumen of halloysite, the small size and amount of the Ag_2O nanoparticles on the outer and edge surface may relate to the low content of silver source. The EDS result (Fig. 2e) for the composite samples confirms the presence of silver and oxygen elements, while the Si and Al elements confirm the matrix halloysite in the composite.

Both the amount and size of Ag_2O nanoparticles in the inner lumen of halloysite can be readily controlled by adjusting the concentration of the Ag^+ in the aqueous silver nitrate solution. For Hal-Ag_2O-1, which was prepared using 0.2 mol/L of silver nitrate, a small amount of Ag_2O nanoparticles averaging 5 nm in size formed in the lumen of halloysite (Fig. 2b). For Hal-Ag_2O-2 prepared using 0.5 mol/L of silver nitrate, the average size of Ag_2O nanoparticles in the lumen increased to 10–15 nm and their abundance increased markedly (Fig. 2c-d). It is noteworthy that the size of Ag_2O nanoparticles in the composites will be restricted by the lumen size of halloysite. The fringes of the Ag_2O nanoparticles show the lattice spacing of 0.203 nm and 0.238 nm (Fig. 2f), corresponding to the (−112) and (200) planes of Ag_2O nanocrystals. This result confirms the nanoparticles in the lumen of halloysite are nanoscale Ag_2O particles.

As Fig. 3a shows, the Ag_2O-NPS agglomerated considerably, resulting in mass that was micrometers in size. When observed under high magnification, evidently this agglomerate is composed of small particles with an average size of ca. 20 nm (Fig. 3b), which is consistent with the result calculated by the Scherrer formula. The circular streaking in the SAED pattern (inset of Fig. 3b) further indicated the agglomerate was composed of randomly orientated, crystalline Ag_2O nanocrystals. From those results, it can be inferred that the prepared composite of Ag_2O and halloysite is able to decrease the coaggregation of Ag_2O nanocrystals due to the spatial confinement of the lumen of halloysite, which could thereby improve the effective surface area of these nanoparticles and augment their reaction activity.

The N_2 adsorption-desorption isotherms for Hal, Hal-Ag_2O-1, and Hal-Ag_2O-2 can all be designated as type IV(a) with H3 hysteresis loops (Fig. 4A, a-c), according to the updated IUPAC classification (Thommes et al., 2015). This type of isotherm is characteristic of mesoporous structures (Yu et al., 2015b). When compared with Hal, both Hal-Ag_2O-1 and Hal-Ag_2O-2 exhibit weakened hysteresis loops, suggesting the diminishment of some mesopores in these halloysite Ag_2O composites. The isotherm of Ag_2O-NPS is best characterized as being a type II isotherm with an insignificant H3 hysteresis loops (Fig. 4A-d); this suggests only a few mesopores existed in Ag_2O-NPS. The PSD curve of Hal revealed two distinct mesoporous populations centered at ca. 2.3 nm and 15.5 nm, respectively (Fig. 4B-a). The former one is ascribed to the slit-shaped longitudinal pores formed during the degassing process, in which the rolled layers of tubular halloysite are separated from each other in response to dehydration of halloysite (Tan et al., 2013). The

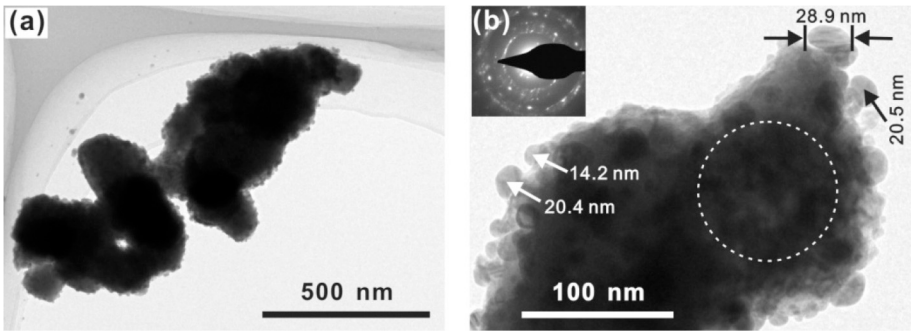

Fig. 3. TEM images of Ag_2O-NPS at low (a) and high (b) magnification. Inset in (b): SAED pattern of the area in the dashed circle.

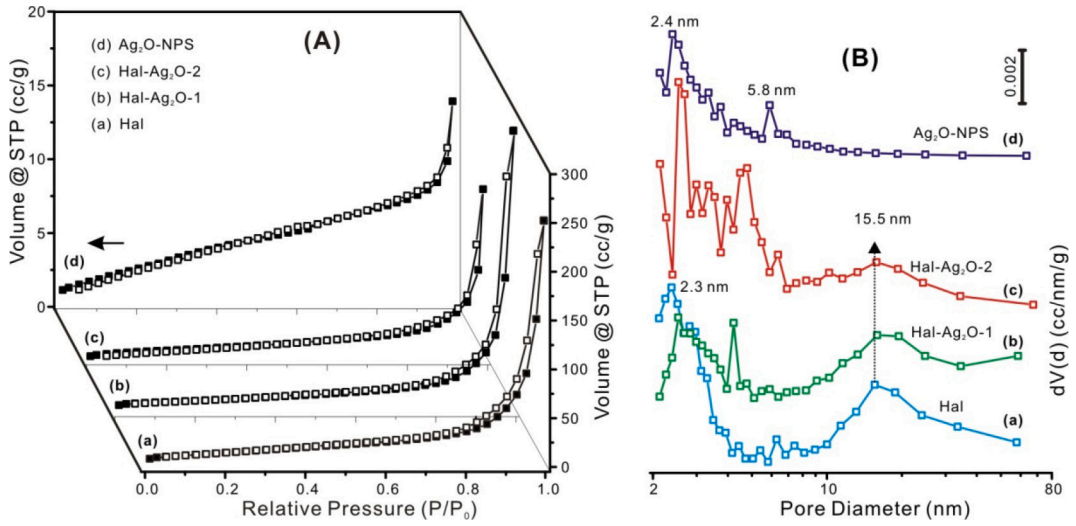

Fig. 4. N_2 adsorption-desorption isotherms (A) and PSD curves (B) of Hal (a), Hal-Ag_2O-1 (b), Hal-Ag_2O-2 (b), and Ag_2O-NPS (d).

latter mesopore population (centered at ca. 15.5 nm) was identified as the lumen of halloysite. Both PSD curves of Hal-Ag_2O-1 and Hal-Ag_2O-2 featured the mesopores populations attributable to slit-shaped longitudinal pores and the lumen of halloysite (Fig. 4B, b-c), but their intensity of the populations at ca. 15.5 nm is lower than that of Hal. This result is best explained by the Ag_2O particles occupying part of the halloysite lumen, such that Hal-Ag_2O-2 sustained a lower mesopore population at ca. 15.5 nm than did Hal-Ag_2O-1 because more Ag_2O particles existed in Hal-Ag_2O-2 (Fig. 2b-d). The mesopore populations from 3 to 5 nm in the PSD curves of Hal-Ag_2O-1 and Hal-Ag_2O-2 could have arisen from the stacking or interval space of Ag_2O particles in the composites, and these kinds of pores should be related to the content of Ag_2O. Indeed, Hal-Ag_2O-2 has more mesopores that ranged from 3 to 5 nm than Hal-Ag_2O-1 (Fig. 4B, b-c), which is probably related to greater Ag_2O content of Hal-Ag_2O-2. As shown in Fig. 2b and c, new nanopores were formed between Ag_2O particles in the lumen or between Ag_2O particles and the inner wall of halloysite in Hal-Ag_2O-2. The PSD curve of Ag_2O displays two mesoporous populations centered at 2.4 nm and 5.8 nm, respectively, which could be derived from the intercrystalline mesopores space.

The S_{BET} of Hal is 56.3 m^2/g, which is higher than those of Hal-Ag_2O-1 and Hal-Ag_2O-2 (Table 1). Two plausible reasons can explain this result: 1) the Ag_2O particles occupy part of the lumen of halloysite, resulting in a decreased S_{BET} of the prepared composites; 2) the Ag_2O has a greater density than that of halloysite and because S_{BET} is the surface area per gram of sample, the composite with Ag_2O should have a lower S_{BET} than does raw halloysite. It was found from Table 1 that Ag_2O-NPS exhibited the lowest S_{BET} value at 11.6 m^2/g, likely because of the significant aggregation of its Ag_2O nanoparticles (Fig. 3) and the high density of Ag_2O. Assuming that silver nitrate filled the pore volume of halloysite and completely converted into Ag_2O during the composite preparation process, the Ag_2O contents per composites, W_s (%), can be estimated from the total pore volume of Hal ($V_{total\text{-}Hal}$, mL/g) and concentration of silver nitrate ($C_{silver\ nitrate}$, mol/L) using the following equation: $W_s = (V_{total\text{-}Hal} \div 1000 \times C_{silver\ nitrate} \times 127)/(V_{total\text{-}Hal} \div 1000 \times C_{silver\ nitrate} \times 127 + 1)$. The calculated W_s values are presented in Table 1; there, the W_s of Hal-Ag_2O-1 is as low as 0.98%. It should be pointed out that these W_s values in Table 1 are underestimated because the outer and edge surfaces of halloysite also retained a small amount of silver nitrate (eventually converted into Ag_2O) during the composite preparation process. This caveat is corroborated by the results of TEM (Fig. 2b-d). The low Ag_2O content of Hal-Ag_2O-1 may help to explain why silver oxide cannot be detected in the XRD pattern.

Table 1
Specific surface area, total pore volume, and Ag_2O contents of the samples.

Samples	S_{BET} (m^2/g)	V_{total} (mL/g)	$C_{silver\ nitrate}$ [a] (mol/L)	W_s [b] (%)
Hal	56.3	0.3902	–	–
Hal-Ag_2O-1	41.3	0.4455	0.2	0.98
Hal-Ag_2O-2	38.8	0.2706	0.5	2.42
Ag_2O-NPS	11.6	0.0215	0.1	–

[a] $C_{silver\ nitrate}$, the concentration of silver nitrate used to prepare the halloysite/Ag_2O composites.
[b] W_s, the silver oxide content of each composite.

3.2. Performance of samples for iodide adsorption

To establish the equilibrium time and determine the kinetics of the adsorption process, I^- adsorption on Hal-Ag_2O-2 was studied as a function of adsorption time. Hal-Ag_2O-2 was chosen for this because of its high Ag_2O content (Table 1). As evinced by Fig. 5a, the adsorption of I^- by Hal-Ag_2O-2 is rapid and can reach equilibrium within 180 min. This fast adsorption ensued because the adsorption mechanism involved is based on the preferable chemical reaction between Ag_2O and I^-. Unlike its chemical adsorption, the physical adsorption of I^- usually takes a longer time to attain the adsorption equilibrium, because, for this mechanism, the adsorption is established by sufficient surface contact and distribution between adsorbent and adsorbate (Sato et al., 2011). In a previous work, the equilibrium time for minerals (such as illite) to physically adsorb I^- is ca. 2 weeks (Kaplan et al., 2000), a significantly longer duration than that demonstrated in the present study. To ensure the adsorption equilibrium was reached, a period of 1440 min was set as the contact time for the following adsorption experiments.

The kinetics curve was fitted using the pseudo-second-order kinetic model (Yuan et al., 2013), whose linear form given by.

$$t/q_t = 1/(kq_e^2) + t/q_e \quad (3)$$

where q_t and q_e (mg/g) are the amount of I^- adsorbed per unit mass of the adsorbent at time t (min) and at equilibrium, respectively, and k (g/mg·min) is the pseudo-second-rate constant of adsorption. As conveyed in Fig. 5b and Table 2, which provide the fitting results, the adsorption of I^- by Hal-Ag_2O-2 fits Eq. (3) quite well. Hence, the kinetics of this adsorption system can be robustly classified as pseudo-second-order, implying that the rate-limiting step may be chemical adsorption.

As shown in Fig. 6a, Hal-Ag_2O-1 is able to remove 96.0% of I^- from the solution with the initial I^- concentration is 0.25 mmol/L, and 100% of I^- can be removed when the initial I^- concentration is 0.1 mmol/L or lower; Hal-Ag_2O-2 is able to remove 78.2% of I^- from the solution with

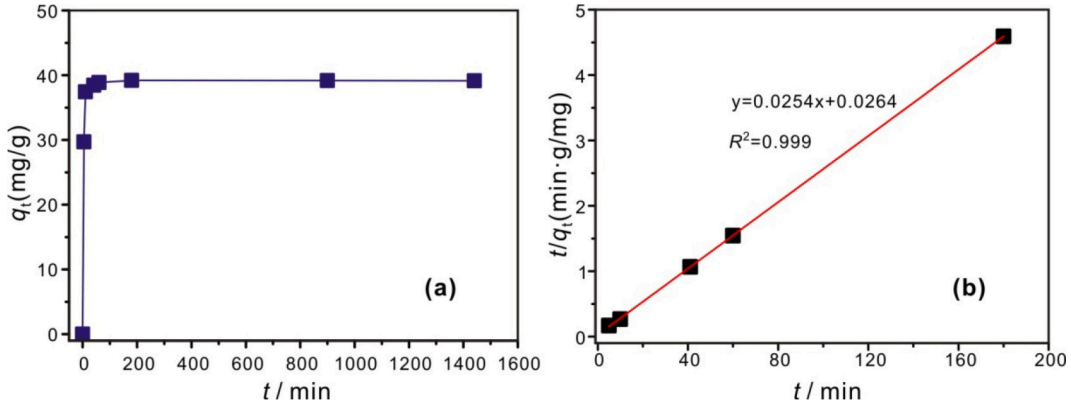

Fig. 5. Adsorption kinetic of I^- on Hal-Ag_2O-2 (a) and the linear fitting plot based on pseudo-second-order kinetic model (b), for an initial I^- concentration of 1.0 mmol/L, at pH = 7.5 ± 0.2.

Table 2
Kinetics constants for Hal-Ag_2O-2 and adsorption capacity of I^- for the different samples.

Kinetics constant		Sample	Q_m (mg/g)	$Q_{m\text{-}s}$ (mg/g)[a]
k (g/mg·min)	0.024	Hal	0.28	–
q_e (mg/g)	39.4	Hal-Ag_2O-1	13.72	1369.50
R^2	0.999	Hal-Ag_2O-2	39.99	1642.36
–	–	Ag_2O-NPS	201.85	–

[a] $Q_{m\text{-}s}$ was calculated based on the following equation: $Q_{m\text{-}s} = (Q_m\text{-}0.28)/W_s$.

an initial I^- concentration of 1.0 mmol/L, and 100% of I^- from solution when the initial I^- concentration is 0.5 mmol/L or lower; however, the I^- removal efficiency of Hal is just less than 4.6% even when the initial concentration of I^- is as low as 0.05 mmol/L. These results strongly indicated that composite formed by Hal and Ag_2O significantly increased the I^- adsorption ability of halloysite.

The adsorption isotherm results revealed that Hal has a very low maximum adsorption capacity (Q_m) to I^-, at 0.28 mg/g, (Fig. 6b, Table 2), which is consistent with previous research that has shown clay minerals to have a negligible I^- adsorption capacity (Yu et al., 1996; Miller et al., 2015), due to the large size and low charge of I^-. However, we recently found chrysotile bundles capable of significant adsorption to I^- with a Langmuir adsorption capacity of 4.13 mg/g, for which the wedge-shape nanopores among the neighboring chrysotile nanotubes were crucial for I^- adsorption (Yu et al., 2019). The Q_m of Hal-Ag_2O-1 and Hal-Ag_2O-2 is 13.72 mg/g and 39.99 mg/g (Fig. 6a, Table 2), which is approximately 48 and 142 times higher than that of Hal, respectively. Further, the Q_m value is higher for Hal-Ag_2O-2 than Hal-Ag_2O-1 (Fig. 6a), which is consistent with the content of Ag_2O in those two composites. This result revealed that the adsorption ability of the prepared composites is strongly related to the Ag_2O contents of the composites. The I^- adsorption capacity of the halloysite/Ag_2O composites prepared in this study was significantly higher than that of other adsorbents (Table S2), such as clay minerals, ferrihydrite, layered double hydroxides, and black carbon (Yu et al., 1996; Liang and Li, 2007; Choung et al., 2013; Miller et al., 2015), making them promising candidates for the removal of I^-.

pH is one of the most important factors that can affect solid-liquid adsorption, and the effect of which on adsorption was usually studied in the literature (Qiu et al., 2018; Li et al., 2020; Yu et al., 2020), because pH can affect the surface nature of adsorbent and also the speciation of adsorbate in solution. In this study, the I^- removal efficiency shows no obvious change in the pH range of 5–9 (Fig. 7a), suggesting the hydrogen ions or hydroxide ions did not affect the adsorption process. The ionic strength also shows no obvious effect on the adsorption of I^- by the prepared composite (Fig. 7a), reflecting a strong affinity between the composite and I^- (Hayes et al., 1987).

As shown by Fig. 7b, the I^- removal efficiency of the halloysite/Ag_2O composites is barely affected by the existence of Cl^-, Br^-, or SO_4^{2-}, even when the concentration of competing anions was 10 times that of iodide ions. This result is explained by the lowest Gibbs energy of the reaction of Ag_2O with I^- than with Cl^-, Br^-, or SO_4^{2-}; hence, the reacting of Ag_2O with I^- is thermodynamically favored over that with Cl^-, Br^-, and SO_4^{2-} (Bo et al., 2013). This result suggests the prepared composite possesses high selective adsorption to I^-.

3.3. Adsorption mechanisms

Both XPS and XRD were used to study the adsorption mechanisms. As

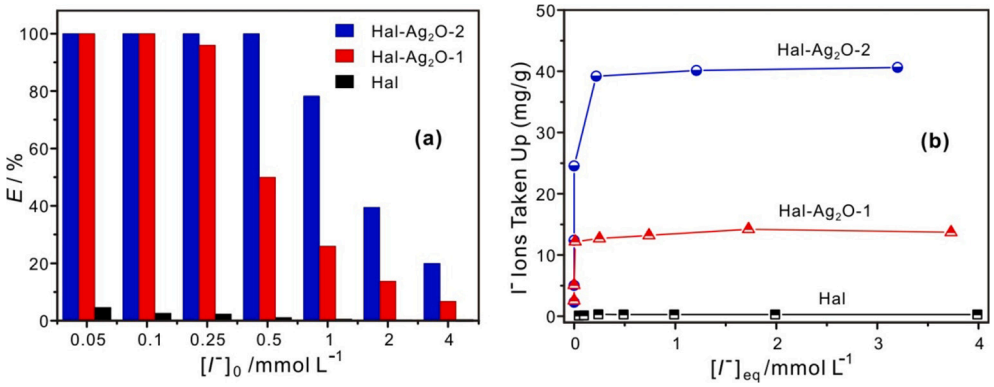

Fig. 6. The I^- removal efficiency, E(%), from solutions with different I^- initial concentrations, solid/liquid ratio = 50 mg/20 mL, pH = 7.5 ± 0.2 (a); Adsorption isotherms of I^- on samples (b).

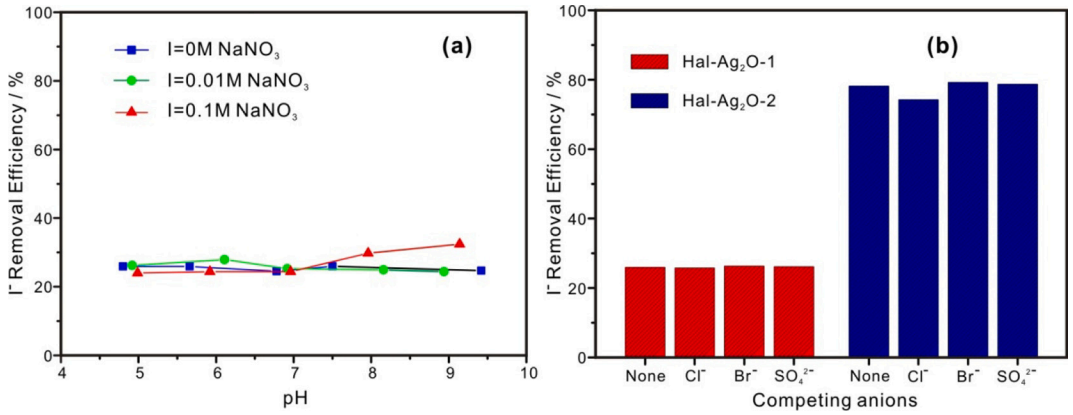

Fig. 7. The effect of pH and ionic strength on I^- adsorption on Hal-Ag_2O-1 (a); I^- removal efficiency of the prepared composite under competitive adsorption (b). Initial I^- concentration 1 mmo/L, Cl^-, Br^-, or SO_4^{2-} concentration of 10 mmol/L, respectively, solid/liquid ratio = 50 mg/20 mL.

seen in Fig. 8a, I3d peaks emerged in the XPS survey scan spectrum after I^- adsorption, qualitatively revealing the presence of iodine in Hal-Ag_2O-2-I. To determine the chemical environment of silver and iodine, high resolution XPS Ag3d and I3d spectra were obtained (Fig. 8b-c). For Hal-Ag_2O-2, the Ag $3d_{5/2}$ peak was located at 368.7 eV (Fig. 8b), which is characteristic for Ag_2O crystals (Liang et al., 2019). Yet after its adsorption of I^-, the Ag $3d_{5/2}$ peak of Hal-Ag_2O-2-I underwent a negative shift with a central binding energy at 368.4 eV (Fig. 8b). This shift indicated that AgI has formed, whose binding energy of Ag $3d_{5/2}$ peak is lower than Ag_2O because of the lower electronegativity of iodine than oxygen. The XPS I $3d_{5/2}$ spectrum of Hal-Ag_2O-2-I confirmed the formation of AgI, by virtue of the characteristic I $3d_{5/2}$ peak at 619.4 eV (Liang et al., 2017). The peaks attributed to AgI were also discernible in the XRD pattern of Hal-Ag_2O-2-I, and the intensity of its peaks assigned to Ag_2O was significantly diminished when compared with those Hal-Ag_2O-2 (Fig. 8d), indicating that part of Ag_2O was converted to AgI after

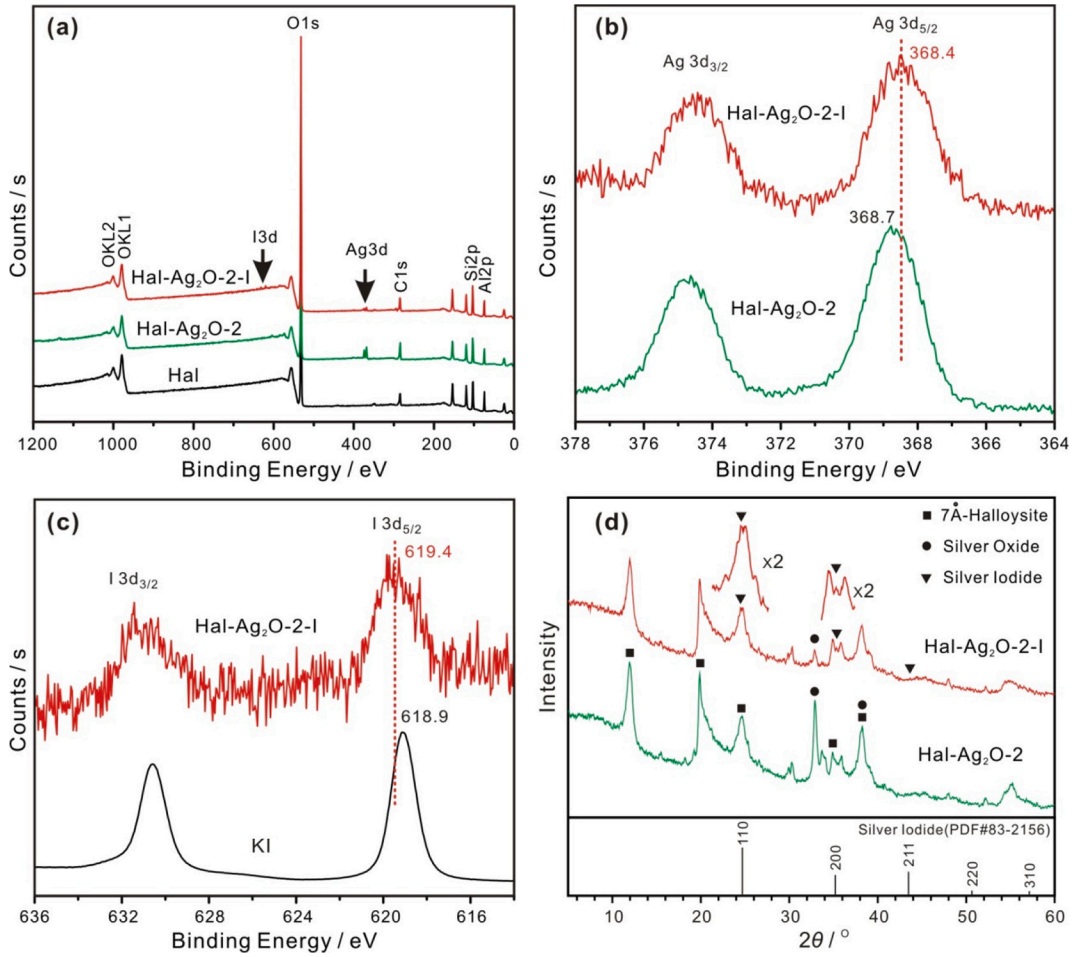

Fig. 8. XPS survey spectra of the halloysite (Hal), halloysite/Ag_2O composite (Hal-Ag_2O-2), and halloysite/Ag_2O composite after adsorption of iodide (Hal-Ag_2O-2-I) (a); high-resolution XPS Ag3d spectra of Hal-Ag_2O-2 before and after adsorption of I^- (b); high-resolution XPS I3d spectra of Hal-Ag_2O-2 after adsorption of I^-, KI was used as a reference (c); XRD patterns of Hal-Ag_2O-2 before and after adsorption of I^- (initial I^- concentration 0.5 mmol/L, 24 h) (d).

the adsorption process. Accordingly, we may surmise the iodide adsorption mechanism is based on this reaction below:

$$2I^-(aq) + Ag_2O + H_2O \rightarrow 2AgI(s) + 2OH^-(aq) \quad (4)$$

According to Eq. (4), the theoretical I^- adsorption capacity per gram of Ag_2O (4.31 mmol) should be 1095.77 mg (8.62 mmol), but we found a much lower Q_m of 201.85 mg/g for Ag_2O-NPS (Table 2). This is because the aggregation of Ag_2O nanocrystals in Ag_2O-NPS decreased the effective surface area and further reduced the efficiency of the Ag_2O nanoparticles. To compare the I^- adsorption efficiency of halloysite/Ag_2O composites with pure Ag_2O, the adsorption capacity normalized to per unit mass (g) of Ag_2O content, $Q_{m\text{-}s}$, was calculated according to values of W_s (Table 1) and Q_m (Table 2). Evidently, the $Q_{m\text{-}s}$ of Hal-Ag_2O-1 is slightly larger than the theoretical adsorption capacity (Table 2). An explanation for this result is the underestimation of W_s, as discussed above. The $Q_{m\text{-}s}$ of Hal-Ag_2O-2 is 1642.36 mg/g (Table 2), also larger than the theoretical adsorption capacity and even larger than that of the Hal-Ag_2O-1. Besides the underestimation of W_s, the newly formed nanopores between Ag_2O particles and the inner wall of halloysite (Fig. 2c-d) may contribute to this high $Q_{m\text{-}s}$ of Hal-Ag_2O-2. This is because the nanopores can significantly modify the mineral-water interface chemistry. For example, the properties of water in nanopores deviate significantly from those of bulk water, in that the density, surface tension, and dielectric constant of water in nanopores were smaller than those of bulk water (Levinger, 2002); in nanopores the surface charge of alumina is modified when compared to alumina particles, leading to a nearly 10-fold increase in surface-normalized adsorption anions on nanoporous alumina (Wang, 2014). Therefore, the aluminum hydroxyl in the newly formed nanopores in the Hal-Ag_2O-2 composite is expected to have the ability to adsorb I^-, whereas the raw halloysite is incapable of adsorption.

Further advantages of the halloysite/Ag_2O composites prepared in this study can be postulated, for example, the composites after capture of the radioactive I^- will likely be of low radiological hazard due to the radioactive I^- primarily sequestered in the lumen of halloysite and because of the shielding of the halloysite wall. For the immobilization of radionuclides, the lattice sites or lattice gaps of a mineral can trap the radioactive anion or cation based on an isomorphism, mineral phase substitution, or eutectic mixture, which has been well studied (Trocellier, 2001; Zhu et al., 2020). Finally, the nanopores or modified nanopores may also have the potential to immobilize radionuclides.

4. Conclusions

In this study, halloysite/Ag_2O composites (Hal-Ag_2O) were prepared with the help of a vacuum process, and the Ag_2O nanoparticles primarily resided in the lumen of halloysite in these composites. The amount and size of Ag_2O nanoparticles in the composites are easily controlled by adjusting the concentration of Ag^+ during the preparation process. Two composites with a ca. 0.98% and 2.42% Ag_2O content (respectively, Hal-Ag_2O-1 and Hal-Ag_2O-2) were successfully prepared. The adsorption of I^- by Hal-Ag_2O-2 with its 2.42% Ag_2O content is rapid and can reach equilibrium within 180 min. The kinetics for adsorption of I^- by Hal-Ag_2O-2 closely followed a pseudo-second-order model. The I^- adsorption capacity of Hal-Ag_2O-1 and Hal-Ag_2O-2 is 13.7 mg/g and 39.99 mg/g, respectively, which is significantly higher than that of raw halloysite (0.28 mg/g). The prepared composites feature high selective adsorption to I^-, and their I^- removal efficiency is hardly impaired by the co-occurrence of Cl^-, Br^-, or SO_4^{2-}, even when the latter's concentration is 10 times that of iodide ions. The composites' high adsorption capacity stems from the small particles size of Ag_2O that is governed by their spatial confinement in the lumen of halloysite as well as the newly formed nanopores between Ag_2O particles and the inner wall of halloysite. Additionally, because Ag_2O mainly resided in the lumen of halloysite, it is expected these composites, once they capture radioactive I^-, will pose a low radiological hazard due to shielding of the halloysite wall. Collectively, these results indicate the halloysite/Ag_2O composites could function as a promising adsorbent material for efficiently removing radioactive I^- from water, and the lumen of halloysite or nanopores of other porous minerals may also harbor some of the potential to immobilize radionuclides.

Declaration of Competing Interest

There are no conflicts of interest to declare.

Acknowledgments

The work was financially supported by the National Natural Science Foundation of China (Grant No. 42072057, 41872046 and 41603065) and Guizhou Provincial Science and Technology Projects (No. ZK[2021] ZD043 and [2019]1318).

Appendix A. Supplementary data

Supplementary data to this article can be found online at https://doi.org/10.1016/j.clay.2021.106241.

References

Abdullayev, E., Sakakibara, K., Okamoto, K., Wei, W., Ariga, K., Lvov, Y., 2011. Natural tubule clay template synthesis of silver nanorods for antibacterial composite coating. ACS Appl. Mater. Interfaces 3, 4040–4046.
Balsley, S.D., Brady, P.V., Krumhansl, J.L., Anderson, H.L., 1996. Iodide retention by metal sulfide surfaces: Cinnabar and chalcocite. Environ. Sci. Technol. 30, 3025–3027.
Barrett, E.P., Joyner, L.G., Halenda, P.P., 1951. The determination of pore volume and area distributions in porous substances. I. Computations from nitrogen isotherms. J. Am. Chem. Soc. 73, 373–380.
Bates, T.F., Hildebrand, F.A., Swineford, A., 1950. Morphology and structure of endellite and halloysite. Am. Mineral. 35, 463–484.
Bichsel, Y., Von Gunten, U., 1999. Oxidation of iodide and hypoiodous acid in the disinfection of natural waters. Environ. Sci. Technol. 33, 4040–4045.
Bo, A., Sarina, S., Zheng, Z., Yang, D., Liu, H., Zhu, H., 2013. Removal of radioactive iodine from water using Ag_2O grafted titanate nanolamina as efficient adsorbent. J. Hazard. Mater. 246, 199–205.
Brunauer, S., Emmett, P.H., Teller, E., 1938. Adsorption of gases in multimolecular layers. J. Am. Chem. Soc. 60, 309–319.
Burton, A.W., Ong, K., Rea, T., Chan, I.Y., 2009. On the estimation of average crystallite size of zeolites from the Scherrer equation: a critical evaluation of its application to zeolites with one-dimensional pore systems. Microporous Mesoporous Mater. 117, 75–90.
Choung, S., Um, W., Kim, M., Kim, M.G., 2013. Uptake mechanism for iodine species to black carbon. Environ. Sci. Technol. 47, 10349–10355.
Decamp, C., Happel, S., 2013. Utilization of a mixed-bed column for the removal of iodine from radioactive process waste solutions. J. Radioanal. Nucl. Chem. 298, 763–767.
Fuge, R., Johnson, C.C., 2015. Iodine and human health, the role of environmental geochemistry and diet, a review. Appl. Geochem. 63, 282–302.
Hayes, K.F., Roe, A.L., Brown, G.E., Hodgson, K.O., Leckie, J.O., Parks, G.A., 1987. In situ X-ray absorption study of surface complexes: Selenium oxyanions on α-FeOOH. Science 238, 783–786.
Hoskins, J.S., Karanfil, T., Serkiz, S.M., 2002. Removal and sequestration of iodide using silver-impregnated activated carbon. Environ. Sci. Technol. 36, 784–789.
Ikari, M., Matsui, Y., Suzuki, Y., Matsushita, T., Shirasaki, N., 2015. Removal of iodide from water by chlorination and subsequent adsorption on powdered activated carbon. Water Res. 68, 227–237.
Joussein, E., Petit, S., Churchman, J., Theng, B., Righi, D., Delvaux, B., 2005. Halloysite clay minerals–a review. Clay Miner. 40, 383–426.
Kaplan, D.I., Serne, R.J., Parker, K.E., Kutnyakov, I.V., 2000. Iodide sorption to subsurface sediments and illitic minerals. Environ. Sci. Technol. 34, 399–405.
Kaplan, D.I., Denham, M.E., Zhang, S., Yeager, C., Xu, C., Schwehr, K., Li, H.P., Ho, Y.F., Wellman, D., Santschi, P.H., 2014. Radioiodine biogeochemistry and prevalence in groundwater. Crit. Rev. Environ. Sci. Technol. 44, 2287–2335.
Levinger, N.E., 2002. Water in confinement. Science 298, 1722–1723.
Li, S., Dong, L., Wei, Z., Sheng, G., Du, K., Hu, B., 2020. Adsorption and mechanistic study of the invasive plant-derived biochar functionalized with CaAl-LDH for Eu(III) in water. J. Environ. Sci. 96, 127–137.
Liang, L., Li, L., 2007. Adsorption behavior of calcined layered double hydroxides towards removal of iodide contaminants. J. Radioanal. Nucl. Chem. 273, 221–226.
Liang, J., Liu, F., Deng, J., Li, M., Tong, M., 2017. Efficient bacterial inactivation with Z-scheme AgI/Bi_2MoO_6 under visible light irradiation. Water Res. 123, 632–641.
Liang, C., Guo, H., Zhang, L., Ruan, M., Niu, C.-G., Feng, H.-P., Wen, X.-J., Tang, N., Liu, H.-Y., Zeng, G.-M., 2019. Boosting molecular oxygen activation ability in self-

assembled plasmonic p-n semiconductor photocatalytic heterojunction of WO_3/Ag@Ag_2O. Chem. Eng. J. 372, 12–25.
Liu, S., Wang, N., Zhang, Y., Li, Y., Han, Z., Na, P., 2015. Efficient removal of radioactive iodide ions from water by three-dimensional Ag_2O–Ag/TiO_2 composites under visible light irradiation. J. Hazard. Mater. 284, 171–181.
Liu, Y., Gu, P., Jia, L., Zhang, G., 2016. An investigation into the use of cuprous chloride for the removal of radioactive iodide from aqueous solutions. J. Hazard. Mater. 302, 82–89.
Liu, X., Pang, H., Liu, X., Li, Q., Zhang, N., Mao, L., Qiu, M., Hu, B., Yang, H., Wang, X., 2021. Orderly porous covalent organic frameworks-based materials: superior adsorbents for pollutants removal from aqueous solutions. Innovation 2, 100076.
Miller, A., Kruichak, J., Mills, M., Wang, Y., 2015. Iodide uptake by negatively charged clay interlayers? J. Environ. Radioact. 147, 108–114.
Morimoto, K., Tamura, K., Umemura, Y., Sato, H., Yamagishi, A., 2011. Capture of radioactive nuclear wastes from sea water by use of clay minerals. Chem. Lett. 40, 867–869.
Ouyang, J., Guo, B.B., Fu, L.J., Yang, H.M., Hu, Y.H., Tang, A.D., Long, H.M., Jin, Y.L., Chen, J., Jiang, J.L., 2016. Radical guided selective loading of silver nanoparticles at interior lumen and out surface of halloysite nanotubes. Mater. Design 110, 169–178.
Pasbakhsh, P., Churchman, G.J., Keeling, J.L., 2013. Characterisation of properties of various halloysites relevant to their use as nanotubes and microfibre fillers. Appl. Clay Sci. 74, 47–57.
Qiu, M., Wang, M., Zhao, Q., Hu, B., Zhu, Y., 2018. XANES and EXAFS investigation of uranium incorporation on nZVI in the presence of phosphate. Chemosphere 201, 764–771.
Sato, I., Kudo, H., Tsuda, S., 2011. Removal efficiency of water purifier and adsorbent for iodine, cesium, strontium, barium and zirconium in drinking water. J. Toxicol. Sci. 36, 829–834.
Shu, Z., Zhang, Y., Yang, Q., Yang, H., 2017. Halloysite nanotubes supported Ag and ZnO nanoparticles with synergistically enhanced antibacterial activity. Nanoscale Res. Lett. 12, 135.
Tan, D.Y., Yuan, P., Annabi-Bergaya, F., Yu, H.G., Liu, D., Liu, H.M., He, H.P., 2013. Natural halloysite nanotubes as mesoporous carriers for the loading of ibuprofen. Microporous Mesoporous Mater. 179, 89–98.
Tan, D., Yuan, P., Annabi-Bergaya, F., Dong, F., Liu, D., He, H., 2015. A comparative study of tubular halloysite and platy kaolinite as carriers for the loading and release of the herbicide amitrole. Appl. Clay Sci. 114, 190–196.
Tanno, K., Liao, X., Kurosawa, F., 1986. Electrolysis of ammonium iodide solution in a Na_2CO_3 I_2 hybrid cycle. Int. J. Hydrog. Energy 11, 463–469.
Theiss, F.L., Ayoko, G.A., Frost, R.L., 2016. Iodide removal using LDH technology. Chem. Eng. J. 296, 300–309.
Thommes, M., Kaneko, K., Neimark, A.V., Olivier, J.P., Rodriguez-Reinoso, F., Rouquerol, J., Sing, K.S., 2015. Physisorption of gases, with special reference to the evaluation of surface area and pore size distribution (IUPAC Technical Report). Pure Appl. Chem. 87, 1051–1069.
Trocellier, P., 2001. Chemical durability of high level nuclear waste forms. In: Annales de Chimie Science des Matériaux. Elsevier, pp. 113–130.
Von Hippel, F.N., 2011. The radiological and psychological consequences of the Fukushima Daiichi accident. Bull. At. Sci. 67, 27–36.
Wang, Y., 2014. Nanogeochemistry: Nanostructures, emergent properties and their control on geochemical reactions and mass transfers. Chem. Geol. 378-379, 1–23.
Wang, X., Chen, L., Wang, L., Fan, Q., Pan, D., Li, J., Chi, F., Xie, Y., Yu, S., Xiao, C., Luo, F., Wang, J., Wang, X., Chen, C., Wu, W., Shi, W., Wang, S., Wang, X., 2019. Synthesis of novel nanomaterials and their application in efficient removal of radionuclides. SCIENCE CHINA Chem. 62, 933–967.
Wei, Y.F., Yuan, P., Liu, D., Losic, D.S., Tan, D.Y., Chen, F.R., Liu, H.C., Zhou, J.M., Du, P. X., Song, Y.R., 2019. Activation of natural halloysite nanotubes by introducing lanthanum oxycarbonate nanoparticles via co-calcination for outstanding phosphate removal. Chem. Commun. 55, 2110–2113.
Welton-Holzer, J., McCarthy, G., Grant-in-Aid, I., 1989. North Dakota State University. ICDD Grant-in-Aid, Fargo, North Dakota, USA.
Wu, S., Qiu, M., Guo, B., Zhang, L., Lvov, Y., 2017. Nanodot-loaded clay nanotubes as green and sustained radical scavengers for elastomer. ACS Sustain. Chem. Eng. 5, 1775–1783.
Yang, D.J., Zheng, Z.F., Zhu, H.Y., Liu, H.W., Gao, X.P., 2008. Titanate nanofibers as intelligent absorbents for the removal of radioactive ions from water. Adv. Mater. 20, 2777–2781.
Yang, D., Sarina, S., Zhu, H., Liu, H., Zheng, Z., Xie, M., Smith, S.V., Komarneni, S., 2011. Capture of radioactive cesium and iodide ions from water by using titanate nanofibers and nanotubes. Angew. Chem. 123, 10782–10786.
Yu, Z., Warner, J.A., Dahlgren, R.A., Casey, W.H., 1996. Reactivity of iodide in volcanic soils and noncrystalline soil constituents. Geochim. Cosmochim. Acta 60, 4945–4956.
Yu, W., Deng, L., Yuan, P., Liu, D., Yuan, W., Chen, F., 2015a. Preparation of hierarchically porous diatomite/MFI-type zeolite composites and their performance for benzene adsorption: the effects of desilication. Chem. Eng. J. 270, 450–458.
Yu, W., Yuan, P., Liu, D., Deng, L., Yuan, W., Tao, B., Cheng, H., Chen, F., 2015b. Facile preparation of hierarchically porous diatomite/MFI-type zeolite composites and their performance of benzene adsorption: the effects of NaOH etching pretreatment. J. Hazard. Mater. 173–181.
Yu, W., Xu, H., Roden, E.E., Wan, Q., 2019. Efficient adsorption of iodide from water by chrysotile bundles with wedge-shaped nanopores. Appl. Clay Sci. 183, 105331.
Yu, W., Xu, H., Tan, D., Fang, Y., Roden, E.E., Wan, Q., 2020. Adsorption of iodate on nanosized tubular halloysite. Appl. Clay Sci. 184, 105407.
Yuan, P., Southon, P.D., Liu, Z., Green, M.E., Hook, J.M., Antill, S.J., Kepert, C.J., 2008. Functionalization of halloysite clay nanotubes by grafting with γ-aminopropyltriethoxysilane. J. Phys. Chem. C 112, 15742–15751.
Yuan, P., Liu, D., Tan, D.Y., Liu, K.K., Yu, H.G., Zhong, Y.H., Yuan, A.H., Yu, W.B., He, H. P., 2013. Surface silylation of mesoporous/macroporous diatomite (diatomaceous earth) and its function in Cu (II) adsorption: the effects of heating pretreatment. Microporous Mesoporous Mater. 170, 9–19.
Yuan, P., Tan, D., Annabi-Bergaya, F., 2015. Properties and applications of halloysite nanotubes: recent research advances and future prospects. Appl. Clay Sci. 112-113, 75–93.
Zeng, X., Wang, Q., Wang, H., Yang, Y., 2017. Catalytically active silver nanoparticles loaded in the lumen of halloysite nanotubes via electrostatic interactions. J. Mater. Sci. 52, 8391–8400.
Zhu, H., Wang, F., Liao, Q., Zhu, Y., 2020. Synthesis and characterization of zirconolite-sodium borosilicate glass-ceramics for nuclear waste immobilization. J. Nucl. Mater. 532.